Advances in Industrial and Manufacturing Engineering 2 (2021) 100049

Contents lists available at ScienceDirect

Advances in Industrial and Manufacturing Engineering

journal homepage: www.journals.elsevier.com/advances-in-industrial-and-manufacturing-engineering

Bi-polynomial fourth-order weld bead model for improved material utilization and accuracy in wire-arc additive manufacturing: A case of transverse twin-wire welding

Manish Kumar [a], S. Surya Kumar [a], Abhay Sharma [b,*]

[a] Department of Mechanical and Aerospace Engineering, Indian Institute of Technology Hyderabad, Sangareddy, 502285, India
[b] KU Leuven, Faculty of Engineering Technology, Department of Materials Engineering, Campus De Nayer, Sint-Katelijne Waver, 2860, Belgium

ARTICLE INFO

Keywords:
Wire-arc additive manufacturing
Twin-wire welding
Overlapping weld bead model
Integrated process and product design

ABSTRACT

With the gradual evolution of metal additive manufacturing (AM) as a viable manufacturing option for realizing complex parts, the research focus has shifted from mere geometric realization to a higher material deposition rate without a significant loss of accuracy. This work aims to demonstrate the potential of traverse twin-wire welding to produce asymmetric weld beads, providing an extra control factor in the weld bead shape and component accuracy while retaining high deposition rates. A new weld bead model - bi-polynomial fourth-order - is developed and linked to the process conditions. The higher-order model is more responsive to the weld bead shape variation and is more accurate than the traditional models. Compared to conventional single polynomial models, which are limited to the symmetrical cross-sectional weld bead, the bi-polynomial model can also simulate the asymmetrical weld bead. The process model of the weld bead and the offset are integrated with the product features to assess the time for fabrication (number of passes) and post-machining material wastage. The usefulness of the integration is demonstrated with the manufacture of a candidate multi-pass multi-layer component. It is envisaged that the investigation will facilitate large-scale wire-arc AM with the use of transverse twin-wire welding.

1. Introduction

The rapid shift in manufacturing from mass production to customized production requires innovation for productivity and quality enhancement. Additive manufacturing (AM) fulfils the immediate demand for complex customized parts with reduced investment in tooling and cycle time. With the maturing of metal AM processes, the focus has shifted from mere feasibility to productivity considerations such as deposition rate. The AM processes that use wire as the feedstock have considerably high deposition rates vis-à-vis, making them suitable for fabricating comparatively large components with high density. Arc welding based deposition processes using gas metal arc welding (GMAW), gas tungsten arc welding (GTAW), or plasma arc welding (PAW) are commonly known as wire-arc additive manufacturing (WAAM. Its distinct advantages – such as high deposition rate, low cost, high efficiency, and strong bonding strength of the parts – make it an ideal process in applications such as pressure vessels, ships, bridge construction, etc. Since its initial realization in the early (Zhang et al., 2003), significant progress has been made in the WAAM process and the mechanical properties and microstructure of the manufactured parts (Wu et al., 2018). The issues of mechanical properties are reasonably resolved through post-heat treatment (Qi et al., 2019) and in-situ cooling (Hackenhaar et al., 2020) or heating (Reddy et al., 2019).

With an increase in demand for large-scale WAAM components, deposition rate requirements will be more demanding. Twin-wire–based systems are capable of providing such high deposition rates. Twin-wire welding uses two electrodes that simultaneously operate in a single weld pool. The twin-wire effectively uses welding heat as the companion arc also heats the wire in a common welding pool. Compared to the twin-wire, multiple welding heads waste heat as the metal melt by the first arc solidifies and reheated by the subsequent arcing. Excess heat increases the residual stress and distortion, which is not the case with the twin-wire process. The twin-wire can be operated in tandem and transverse orientations. In the tandem mode (Fig. 1a), the wires follow the weld seam. On the other hand, if the two wires remain beside each other in a plane perpendicular to the welding direction, the orientation is known as a

* Corresponding author.
E-mail address: abhay.sharma@kuleuven.be (A. Sharma).

https://doi.org/10.1016/j.aime.2021.100049
Received 24 October 2020; Received in revised form 16 April 2021; Accepted 25 April 2021

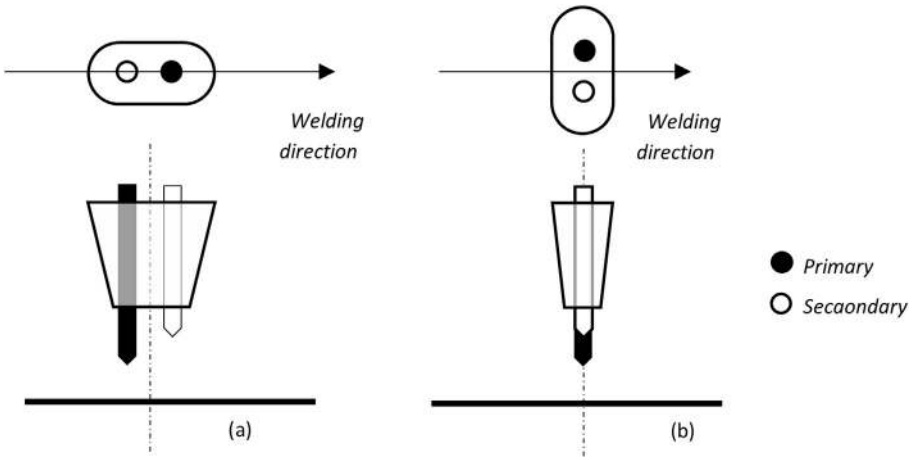

Fig. 1. Wire orientation in twin-wire welding: (a) tandem and (b) transverse.

transverse orientation (Fig. 1b).

In the last decade, the GMAW version of twin-wire arc welding has been proven for its stable welding operations with the individual control of currents at the two power sources with a time gap. These two sources are commonly termed primary–secondary or master-slave power sources. The power sources are anti-phased and synchronized so that only one arc ignites at a given point in time. The arc first ignites at the electrode connected to the primary source, followed by arcing at the secondary electrode. This arrangement prevents the mutual disturbance of the arcs. The difference between the primary and secondary currents induces stability in the arcs (Moinuddin et al., 2015). The fundamental difference in arcing with the tandem and transverse modes is that the trailing electrode in tandem orientation acts on the turbulent weld pool produced by the leading electrode. On the contrary, the trailing wire in transverse mode acts on the solid plate heated by the leading electrode. The hot plate eases the electron emission and improves overall arc stability (Kumar et al., 2020). The lead and trail electrodes ignite in the overlapping but individual weld pool. The weld pool grows in size at a higher value of the current and eventually merges.

In recent years, tandem twin-wire welding has been reported for use in WAAM. The work of Martinal et al. (2019) showed the feasibility of achieving a high deposition rate of 9.5 kg/h in martensitic stainless steel (Martina et al., 2019). The investigation emphasized a need for external cooling for the control of the material flow. The observations of Shi et al. (2019a) were similar, wherein tandem GMAW with active cooling increased the wire feed speed by 9%–15% and reduced the inter-layer dwell time by 42%–54%. Feng et al. (2018) fed a plasma arc with a double-wire feed for WAAM in Cr–Ni stainless steel. Compared to a single wire feed, the double wire feed enhanced the deposition rate 1.06 times, while the ultimate tensile strength and elongation increased by 176% and 10.2%, respectively. Tandem wires with different wire compositions have also been experimented with for use in AM, e.g. Al–Cu and Al–Mg wires (Gu et al., 2018). However, the wire combination resulted in micro-cracks that propagated to the partially melted zone. Qi et al. (2018) mitigated the lack of mechanical properties in additively manufactured Al-6.3Cu alloy by feeding magnesium into Al–Cu welds with double-wire WAAM. The twin cold metal transfer (CMT Twin) is recently reported for the additive manufacture of nickel aluminium bronze components (Queguineur et al., 2020). The weaving of the CMT twin assists in widening the bead and controls generation at the surface. The tandem twin wire is also useful in manufacturing the multi-node trajectory with minimum welding torch adjustment (Shi et al., 2019b).

Despite the twin-wire AM potentials, the trade-off is that the deposition rate increases the constituent weld bead's size, the geometrical inaccuracies, and the buy-to-fly ratio (weight of the deposited component divided by the weight of the final component). The welding parameters produce a significant effect on weld bead geometry., e.g. the welding current has a significant effect on the appearance of a single bead and a multi-layer single pass in GMAW-based AM parts (Xiong et al., 2015). It is indispensable to establish a bead geometry model which can relate welding process parameters to bead geometry and is used in process control (Li et al., 2020). Several reported welding process models could predict weld bead shape attributes, viz., height (h), width (w), and reinforcement area. These attributes are used to describe the bead shape (cross-section) using standard mathematical curves, e.g. circular segment (Dutta et al., 2008; Aiyiti et al., 2006), parabola (Cui, 2007: Suryakumar et al., 2011), Gaussian, logistic, and sine functions (Cao et al., 2011), and cosine curve (Xiong et al., 2013; Ding et al., 2015a).

The preceding bead profile models were fit in the beads produced by single-wire welding, wherein the bead is bound to be symmetric to the mid-plane of the weld bead cross-section. The tandem orientation of two wires also produces a symmetric weld bead (Fig. 2 (a)). The transverse orientation induces asymmetry in the weld shape, particularly when the primary and secondary currents are different (Fig. 2b) and/or the torch is inclined (Fig. 2c).

Traverse twin-wire welding provides an extra control factor in weld bead shape and component accuracy while retaining high deposition rates. Various bead profiles and their predictive models have been explored for single-wire GMAW; however, twin-wire GMAW has not been similarly examined. Few twin-wire bead models include the twin-wire submerged arc weld bead model (Sharma et al., 2015) and the twin-wire GMAW model for similar and dissimilar welding (Somashekara et al., 2017), both in tandem orientation. The single-wire weld bead studies point to the prevalence of a symmetric cross-section of beads and the untapped potential of asymmetric weld beads in the geometric control. Compared to beads' symmetric cross-section, the moot point is that asymmetric beads (skewed) can better fit the desired component profile, thus offering better accuracy and an improved buy-to-fly ratio. Such an asymmetric bead is highly likely when the twin wire is used in the transverse orientation, particularly with different currents at the two electrodes (Fig. 2b) or an inclined torch (Fig. 2c). Concurrently, the difference in primary and secondary currents provides a thermodynamically stable condition that leads to enhanced arc stability and change in microstructure (Moinuddin et al., 2016).

This work aims to analyze the weld bead profile and present a predictive weld bead model for twin-wire transverse GMAW in the framework of AM. The goal is to fine-tune the weld bead's shape without compromising on the deposition rate, making traverse twin-wire additive manufacturing (T^2WAAM) the ideal process for consideration. The article aims to present an overlapping asymmetric weld bead model for creating a given layer, as flat as possible, to act as a substrate for the next layer. The weld bead model is further used to integrate the product and process

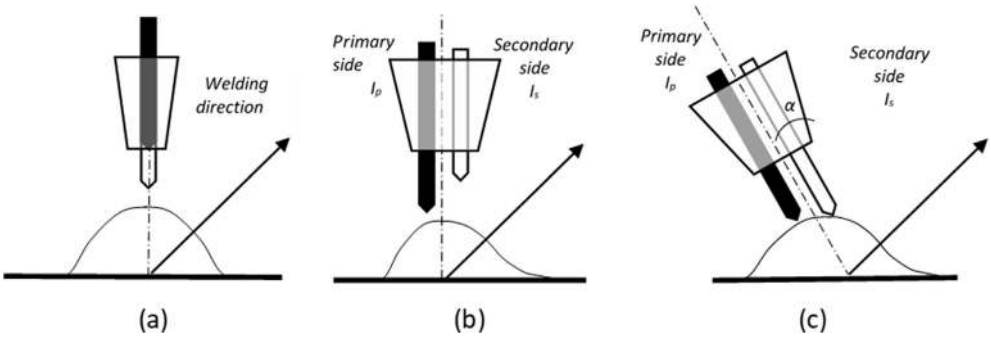

Fig. 2. Weld bead profiles – (a) symmetric and (b and c) asymmetric – caused by tandem and transverse orientations.

design of WAAM. Therefore, the efficacy of the twin-wire transverse process is demonstrated at a component level. Through the integrated product and process model, the article also presents a method to divulging the effect of the process parameters on the number of passes and layers (a process aspect) and the material wastage (a product aspect) through a case study on a candidate object.

2. Experimental details

The AM components are multi-pass multi-layered. A desired component can be realized in a layer-by-layer (multi-layer) manner, with each layer comprising overlapping weld beads (multi-pass). Hence, the weld bead shape has a significant effect on each layer and the component's resultant cumulative geometry. Hence, the first stage of the work is an analysis of the fundamental block, viz., the asymmetric weld bead geometry. The experiments were performed using twin-wire robotic GMAW having two separate welding power sources: primary and secondary. Fig. 3a shows the experimental setup. The weld beads were laid transversely, i.e. the wires were aligned perpendicular to the welding direction, as shown in Fig. 3b.

Weld beads and layers were deposited following the welding conditions listed in Table 1. The range of primary and secondary welding currents was determined by visual inspection of the weld beads. Inclination angles 0° and 15° were chosen from the preliminary experiments. A reasonable difference in the bead shape was observed when the torch is tilted about 15° beyond which visually sound welds were not observed. A representative weld bead and a layer are shown in Fig. 4a and b, respectively. The beads and layers were 3D scanned images (Figs. 4c and 3d). A MATLAB code was written to digitize the weld bead cross-section and bead overlapping surface profile at the middle of the weld length. The digitized data were used to calibrate the twin-wire weld bead model for AM. The weld bead model is employed to obtain the process planning (number of layers and beads) required to deposit a block with a trapezoidal cross-section, as mentioned in Section 3.3 and shown in Fig. 14.

Table 1
Experimental conditions.

Ip (A)	*Is* (A)	Torch Angle (α)
140	140	0° and 15°
160	140	0° and 15°
160	160	0° and 15°
180	140	0° and 15°
180	160	0° and 15°
180	180	0° and 15°
200	140	0° and 15°
200	160	0° and 15°
200	180	0° and 15°
200	200	0° and 15°
220	140	0° and 15°
220	160	0° and 15°
220	180	0° and 15°
220	200	0° and 15°
220	220	0° and 15°
140	160	15°
140	180	15°
140	200	15°
140	220	15°
160	180	15°
160	200	15°
160	220	15°
180	200	15°
180	220	15°
200	220	15°

3. Twin-wire bead model for AM

Curves such as parabolic, elliptical, circular, cosine, and polynomial, as reported in the literature, do not fit into an asymmetric weld bead

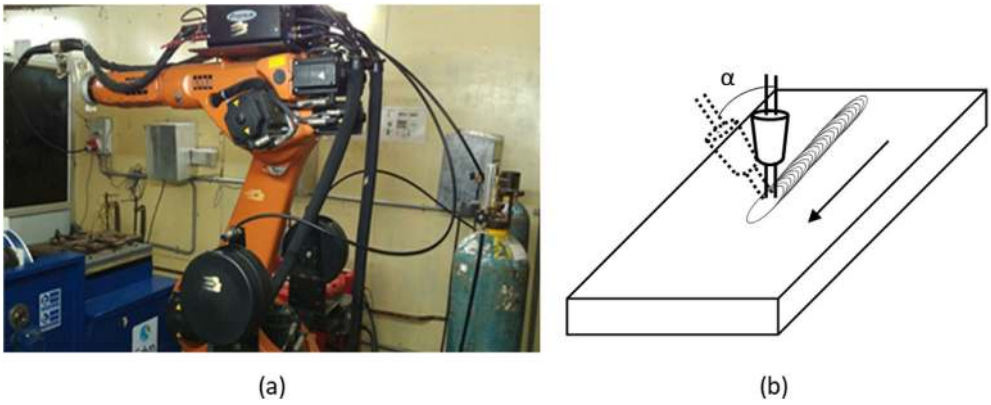

Fig. 3. Experimental setup – (a) welding unit and (b) transverse wire welding with torch inclination.

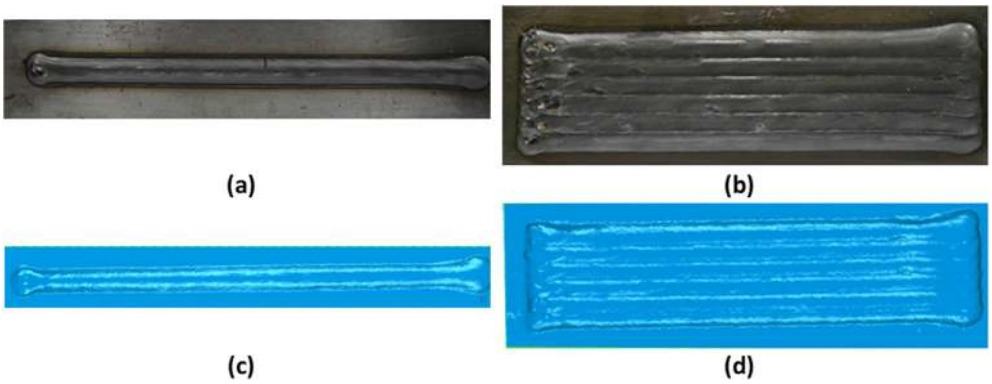

Fig. 4. Actual and laser 3D scan weld bead (a and c) and weld layer (b and d).

profile of transverse twin-wire welds. A typical twin-wire transverse weld, as can be seen in Fig. 5, is asymmetrical in shape. As a result, the weld bead on the primary and secondary sides can be represented by different characteristic curves, merging at the peak and having a common height equal to the weld bead's height. Each of these curves is captured in the form of a generic polynomial function, avoiding any type of predisposition about their shape.

3.1. Asymmetric bead model

Let the bead widths along the primary and secondary sides be denoted as w_p and w_s, respectively. The bi-polynomial curves ($f_p(x)$ and $f_s(x)$) of the nth order degree represent the primary and secondary sides of the weld bead profile, as shown in Fig. 4, and given as follows:

$$f_p(x) = a_{0p} + a_{1p}x + a_{2p}x^2 + \cdots\cdots\cdots + a_{np}x^n \quad (1)$$

$$f_s(x) = a_{0s} + a_{1s}x + a_{2s}x^2 + \cdots\cdots\cdots + a_{ns}x^n \quad (2)$$

Here, the x-axis is along the base plate's surface, with its centre located at the point of maximum height, as shown in Fig. 5. Thus, the polynomials must satisfy the following conditions:

$$f_p(0) = f_s(0) = h \quad (3)$$

Condition 3 leads to $a_{0p} = a_{0s} = h$; therefore:

$$f_p(x) = h + a_{p1}x + a_{p2}x^2 + \ldots\ldots\ldots\ldots + a_{pn}x^n \quad (4)$$

$$f_s(x) = h + a_{s1}x + a_{s2}x^2 + \ldots\ldots\ldots\ldots + a_{sn}x^n \quad (5)$$

The coefficients (a_p and a_s) are obtained via the m-point method for the nth order polynomial. In this method, the weld half-width is divided into (m) parts (m > n), and the weld height at each division is measured, as shown in Fig. 6. For uniform representation, (m−1) parts can be equally spaced, which would yield bead heights at different parts for the primary and secondary sides (where subscript (.) represents the attributes of the primary or secondary side), as follows:

$$y_{1.} = h + a_{1.}\left[\frac{w_.}{m}\right] + a_{2.}\left[\frac{w_.}{m}\right]^2 + \ldots\ldots\ldots\ldots + a_{n.}\left[\frac{w_.}{m}\right]^n \quad (6.1)$$

$$y_{2.} = h + a_{1.}\left[\frac{2w_.}{m}\right] + a_{2.}\left[\frac{2w_.}{m}\right]^2 + \ldots\ldots\ldots\ldots + \left[\frac{2w_.}{m}\right]^n \quad (6.2)$$

$$\vdots \quad \vdots \quad \vdots \quad \vdots \quad \vdots \quad \vdots \quad \vdots$$

$$y_{i.} = h + a_{1.}\left[\frac{iw_.}{m}\right] + a_{2.}\left[\frac{iw_.}{m}\right]^2 + \ldots\ldots\ldots\ldots + a_{n.}\left[\frac{iw_.}{m}\right]^n \quad (6.i)$$

$$\vdots \quad \vdots \quad \vdots \quad \vdots \quad \vdots \quad \vdots \quad \vdots$$

$$y_{m.} = h + a_{1.}w_. + a_{2.}w_.^2 + \ldots\ldots\ldots\ldots + a_{n.}w_.^n \quad (6.n)$$

Eq. 6 can be expressed in matrix form as follows:

$$Y_. = \beta_. X_. \quad (7)$$

where

$$Y_. = \begin{bmatrix} y_{1.} - h \\ y_{2.} - h \\ . \\ y_{i.} - h \\ . \\ y_{m.} - h \end{bmatrix} \quad (8)$$

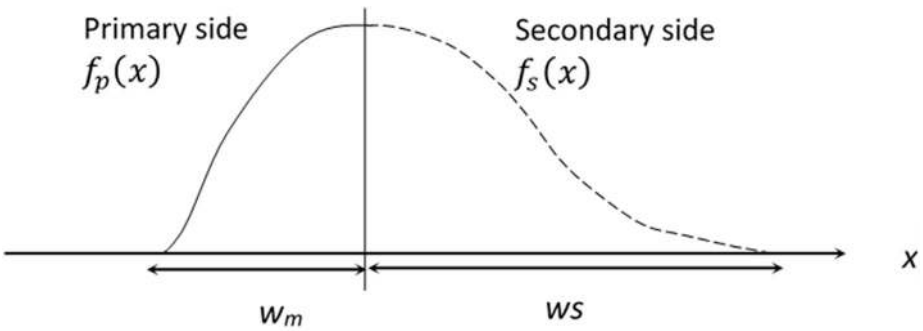

Fig. 5. Bi-polynomial model for asymmetric weld bead.

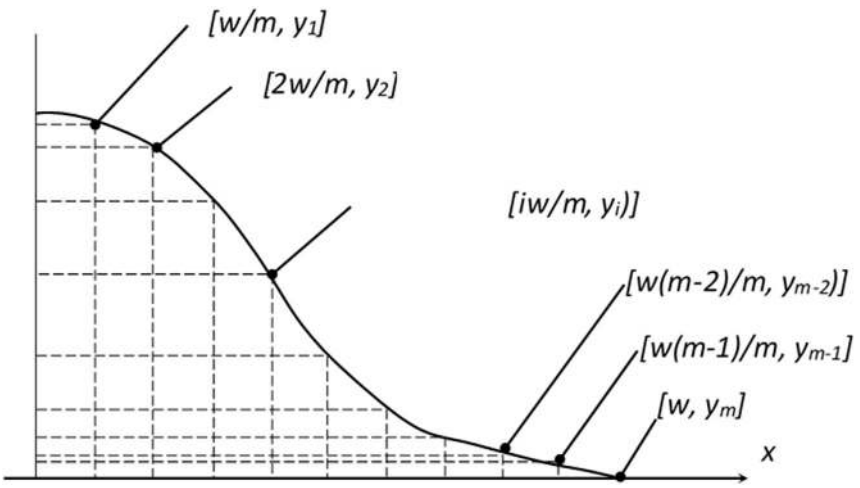

Fig. 6. M-point method for the calculation of coefficients.

$$X_{.} = \begin{bmatrix} \left[\frac{w_{.}}{m}\right] & \left[\frac{w_{.}}{m}\right]^2 & \cdots & \left[\frac{w_{.}}{m}\right]^j & \cdots & \left[\frac{w_{.}}{m}\right]^n \\ \left[\frac{2w_{.}}{m}\right] & \left[\frac{2w_{.}}{m}\right]^2 & \cdots & \left[\frac{2w_{.}}{m}\right]^j & \cdots & \left[\frac{2w_{.}}{m}\right]^n \\ \cdots & \cdots & \cdots & \cdots & \cdots & \cdots \\ \left[\frac{iw_{.}}{m}\right] & \left[\frac{iw_{.}}{m}\right]^2 & \cdots & \left[\frac{iw_{.}}{m}\right]^j & \cdots & \left[\frac{iw_{.}}{m}\right]^n \\ \cdots & \cdots & \cdots & \cdots & \cdots & \cdots \\ w_{.} & w_{.}^2 & \cdots & w_{.}^j & \cdots & w_{.}^n \end{bmatrix} \tag{9}$$

$$\beta_{.} = [a_{1.} \quad a_{2.} \quad \ldots \quad a_{3.} \quad \ldots \quad a_{n.}]^T \tag{10}$$

Based on Eq. (7), the coefficient matrix $\beta_{.}$ can be obtained as follows:

$$\beta_{.} = Y_{.}X_{.}'(X_{.}X_{.}')^{-1} \tag{11}$$

The coefficients of Eqs. (4) and (5) can be validated by their ability to predict the weld bead shape and thereby the weld width and weld area on the primary and secondary sides. Once the bead's bi-polynomial profile is known, an overlapping model of the adjacent asymmetric beads can be developed and used to design the WAAM process.

3.2. Overlap model of adjacent asymmetric beads

The WAAM-based deposition process involves continuous overlapping beads for the fabrication of a bulk component. Unlike single-wire welding, an asymmetric bead is expected in this case of wires' transverse orientation. Therefore, the existing overlap models for symmetrical weld beads are not applicable. However, the underlying assumption in all of them that the overlap volume of the material fills the valley between the two beads can also be true in this case. A simple sketch of the overlapping model, as shown in Fig. 7, depicts the area of the valley and the overlapping areas in the adjacent beads. The peak-to-peak distance between the adjacent beads (i.e. offset) is *d*.

To conserve the volume and assuming that the excess material fills the valley in a flat manner (B1FB2) in Fig. 7, the areas can be written as follows:

$$Area(AB_1B_2) = Area(AC_1A_2) \tag{12}$$

$$Area(AFB_1) + Area(AFB_2) = Area(AEA_2) + Area(AEC_1) \tag{13}$$

Assuming the origin at D1, Eq. (13) can be rewritten as follows:

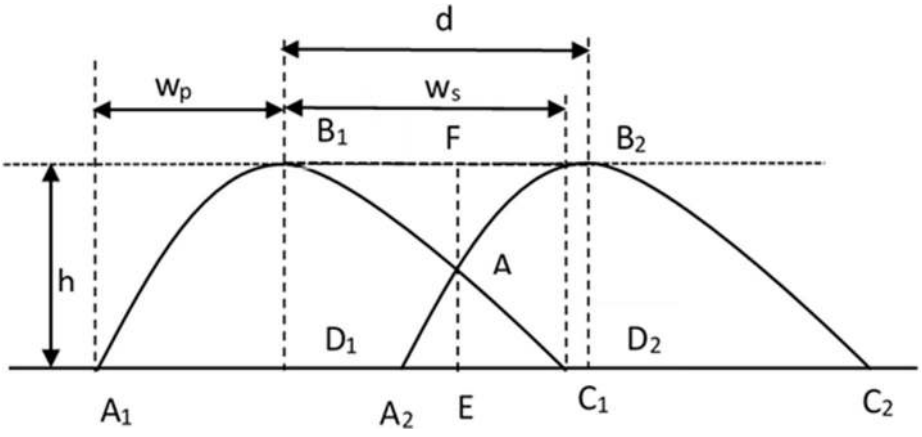

Fig. 7. Overlapping of the asymmetric weld bead.

$$\int_0^{x_E}(h-f_s(x))dx+\int_{x_E}^{d}\big(h-f_p(x-d)\big)dx=\int_{d-w_p}^{x_E}f_p(x-d)dx+\int_{x_E}^{w_s}f_s(x)dx \quad (14)$$

where $x_e = AE$.

$$\int_0^{x_E}hdx-\int_0^{x_E}f_s(x)dx+\int_{x_E}^{d}hdx-\int_{x_E}^{d}f_p(x-d)dx=\int_{d-w_p}^{x_E}f_p(x-d)dx+\int_{x_E}^{w_s}f_s(x)dx \quad (15)$$

$$\int_0^{x_E}hdx+\int_{x_E}^{d}hdx-\int_0^{x_E}f_s(x)dx-\int_{x_E}^{w_s}f_s(x)dx-\int_{x_E}^{d}f_p(x-d)dx-\int_{d-w_p}^{x_E}f_p(x-d)dx=0 \quad (16)$$

$$\int_0^{d}hdx-\int_0^{w_s}f_s(x)dx-\int_{d-w_p}^{d}f_p(x-d)dx=0 \quad (17)$$

$$\int_0^{d}hdx-\int_0^{w_s}f_s(x)dx-\int_{-w_p}^{w_p}f_p(x)dx=0 \quad (18)$$

On solving Eq. (18),

$$d=w_s-w_p+\frac{1}{h}\left[\frac{a_{1s}{w_s}^2+a_{1p}{w_p}^2}{2}+\frac{a_{2s}{w_s}^3-a_{2p}{w_p}^3}{3}+\frac{a_{3s}{w_s}^4+a_{3p}{w_p}^4}{4}+\cdot\cdot+\cdot\frac{a_{ns}{w_s}^{n+1}+a_{np}\left(-w_p\right)^{n+1}}{n+1}\right] \quad (19)$$

$$d=w_s-w_p+\frac{1}{h}\sum_{i=1}^{n}\frac{a_{is}{w_s}^{i+1}+a_{ip}\left(-w_p\right)^{i+1}}{i+1} \quad (20)$$

The estimation of d enables the calculation of the number of passes required to build a product. The first and last weld beads in the multi-pass layer are responsible for creating a product's lateral surface. The surface topography determines the buy-to-fly ratio through the material loss that occurs during post-machining.

3.3. AM process design

The model presented in the earlier section for determining the offset distance d between two beads can be scaled up across the layers to design the process model for the whole component by estimating the number of weld runs and material wastage. A representative case of an AM-manufactured block with a trapezoidal cross-section (Fig. 8) is presented in this section to illustrate this approach. The trapezoidal cross-section has a base width B, a height H, and a wall angle θ. To ensure adequate material distribution during finish machining, every layer needs to be deposited with extra width to support the subsequent layer.

The total number of weld runs required to produce an i^{th} layer of the block can be obtained as follows:

$$width\ of i^{th}\ layer = B-(i-1))2h\cot\theta \quad (21)$$

$$number\ of\ weld\ runs\ in\ i^{th}\ layer=\frac{B-\ (i-1)\ 2h\cot\theta}{d}+1 \quad (22)$$

where represents the rounding up to the next integer. The addition of 1 in Eq. (22) takes care of the half-width at the edges that does not support the next layer.

$$number\ of\ layers = l=\frac{H}{h} \quad (23)$$

$$total\ number\ of\ weld\ runs = N=\sum_{1}^{l}\left[\frac{B-\ (i-1)2h\cot\theta}{d}+1\right] \quad (24)$$

The actual and theoretical cross-sections of the deposited material (V_a and V_t, respectively) for the trapezoidal geometry (Fig. 7) can be calculated as follows:

$$V_a=N^*\left(A_p+A_s\right) \quad (26)$$

$$V_t=(B-H\cot\theta)\ H \quad (27)$$

The % material waste (M_w) in post-machining is calculated as follows:

$$M_w=\frac{V_a-V_t}{V_a}*100 \quad (28)$$

$$M_w=\frac{N^*A-(B-H\cot\theta)H}{N^*A}*100 \quad (29)$$

The material waste can be related to the buy-to-fly ratio if the loss

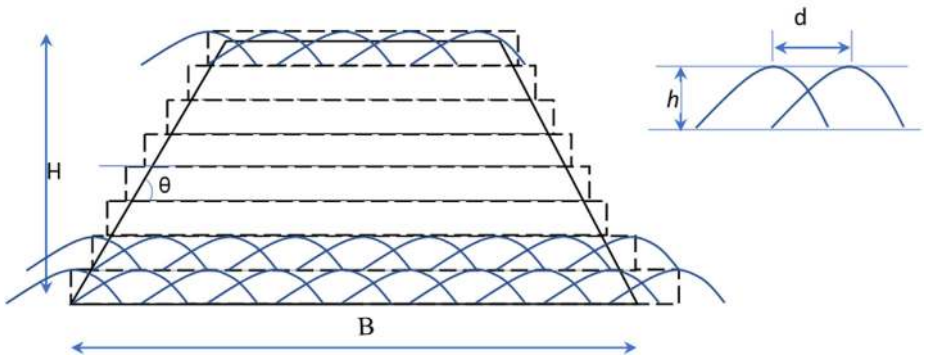

Fig. 8. Cross-section schematic of the trapezoidal block.

from metal evaporation and spatter is known. The loss depends on the welding process and process conditions; for instance, in twin-wire submerge arc welding, this loss may vary from 4% to 8% (Sharma et al., 2008a). The data on metal evaporation and spatter loss in the GMAW version of twin-wire welding are unknown; however, the cold metal transfer–based GMAW process variants (single and twin) are claimed to have a negligible spatter loss. Assuming that no evaporation and spatter loss occurs, the buy-to-fly ratio is equal to V_a/V_t, which relates to the post-machining material loss in Eq. (29).

In addition to the machining of the lateral surfaces, the start and end of an open path deposition also need to be removed. The start and end of a weld bead extend beyond the intended weld length (robot motion), as shown in Fig. 4a. The extension is almost consistent (between 8 and 10 mm) for all the tested conditions. Furthermore, this extension becomes non-existent for the closed path deposition and is not considered for material loss calculation. For the open path deposition, the end loss can further be curtailed by alternating the welding direction after each deposition layer. As this work's focus is on the weld bead shape, other parameters were not significantly altered. However, the user may keep in mind that the proper selection of d, h, A_S, and A_p in Eqs. (24) and (28) can further optimize the total number of weld runs and material wastage.

4. Results and discussion

4.1. Selection of polynomial function and validation

The second-, third-, and fourth-order polynomials are fit in transverse twin-wire beads. The shape of the weld bead fits the fourth-order binominal curves (Fig. 9d). The traditional flat model (second-order equation; parabola) and the critical valley model (second-order model with an additional constant term, Ding et al., 2015a) are unsuitable for twin-wire transverse-bead. Therefore, a generic higher-order model is introduced. The second-order (Fig. 9b) and third-order (Fig. 9c) polynomials under-predict or over-predict the bead height and the bead width. The polynomial coefficients representing beads for different welding conditions (Table 1) are obtained by Eq. (12). The coefficients are given in Appendix 1. The minimum of absolute real roots of polynomials indicates weld widths on the primary and secondary sides. Fig. 10 compares the effectiveness of the third- and fourth-order polynomials in terms of the weld widths' predictability. The fourth-order polynomial predicts the weld width on the primary and secondary sides within a ±10% error band (Fig. 10b). On the contrary, several cases fall beyond the ±10% error band when the third-order polynomials are considered.

4.2. Analysis of weld bead height, width, area, and offset

The effect of currents (I_p and I_s) and torch orientation (α) on weld bead characteristics (h, w, A_s, A_p, w_s, and w_p) and bead critical offset (d) are analyzed in two ways. First, the effects of the sum of welding currents I_p and I_s on bead height, bead width, bead area, and offset – as shown in Fig. 11a, b, 11c, and 11d, respectively – are analyzed. The sum of the currents represents the total heat supplied collectively by the two electrode wires. Second, the effect of the difference in welding currents I_p and I_s is analyzed, as shown in Fig. 12. The difference in current signifies the arc stability, as discussed earlier. For WAAM and in general, for the welding process with single-wire GMAW, the increases in bead height (Fig. 11a), width (Fig. 11b), and bead area (Fig. 11c) with an increase in the current are well documented. Furthermore, as a thumb rule $^2/_3$ of the weld width, the offset also increases with the current. A comparable result is also evident for transverse twin-wire GMAW welds with some variation because of torch inclination.

The bead height is categorically higher with a 15° torch orientation. The bead width is sensitive to the change in the torch angle. The width varies over a wide range with a 15° torch orientation (Fig. 11b). However, the maximum possible width within the range of experiments is almost the same for the 0° and 15° torch orientations. The bead area increases with torch inclination (Fig. 11c), while the offset distance marginally increases for the weld obtained at a higher inclination

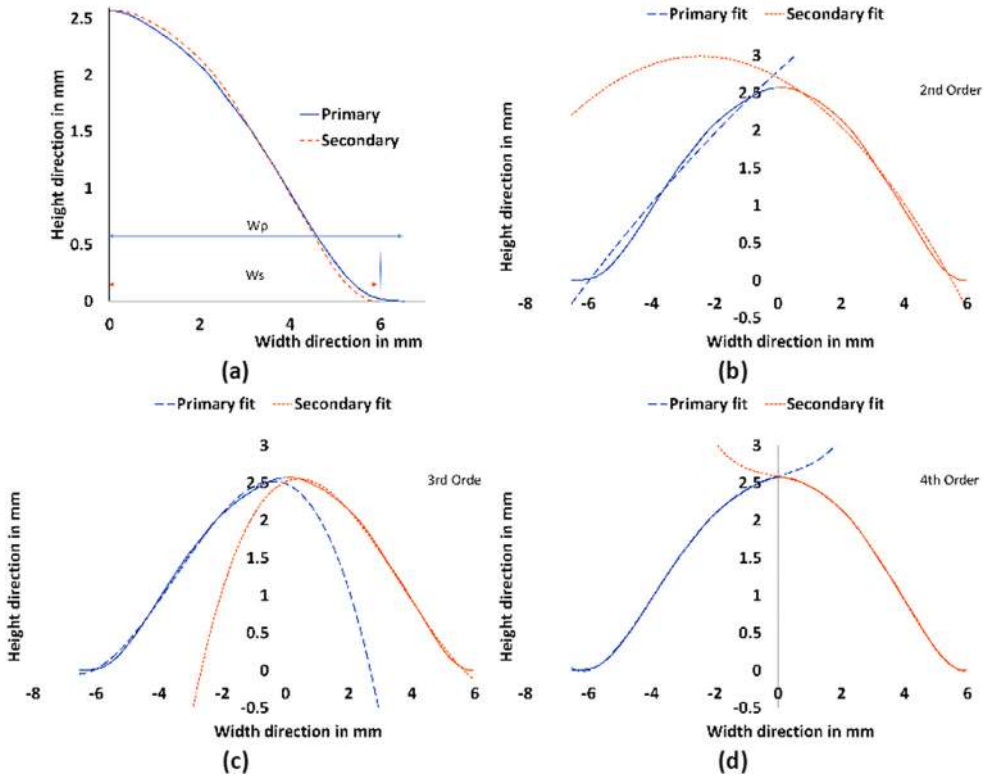

Fig. 9. Comparison of bead shape on primary and secondary sides (a) and fitting of polynomials in bead shape in the (b) second-order, (c) third order, and (d) fourth-order.

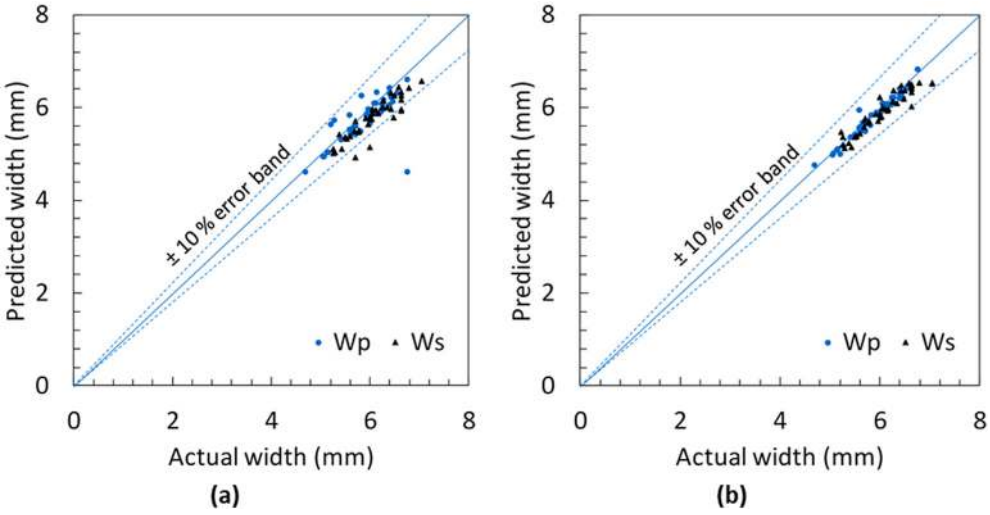

Fig. 10. Comparison of (a) third- and (b) fourth-order polynomials.

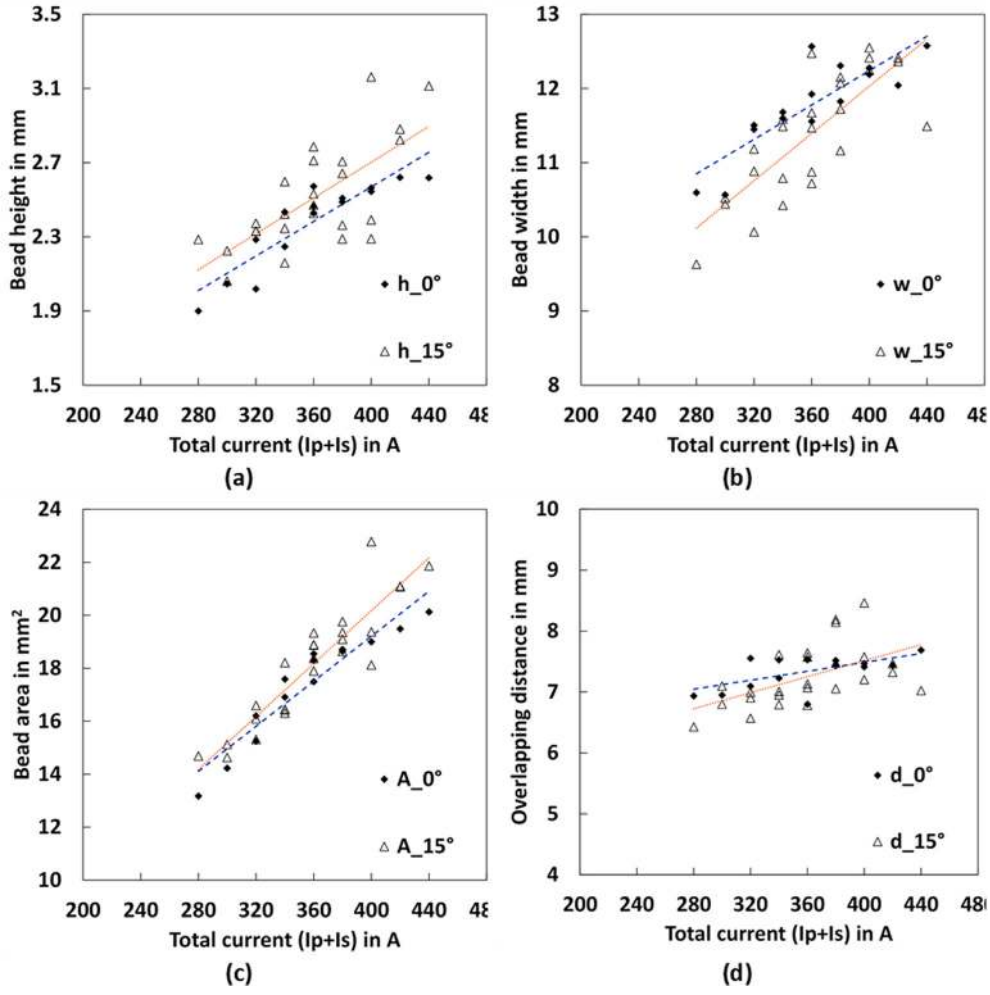

Fig. 11. Effect of welding parameters and electrode inclination.

(Fig. 11d).

The torch is inclined towards the primary current. This inclination increases the CTWD on the secondary side and reduces the same on the primary side. The change in CTWD changes the electrode extension length, responsible for joule heating as the electrical resistance increases with the bare electrode's length. The twin-wire arrangement offers a complex interaction between the electrodes. Not only the current but also the relative difference between the current values influences the arcing phenomenon. The difference in currents at the primary and secondary electrodes induces arc stability because of the electromagnetic field's

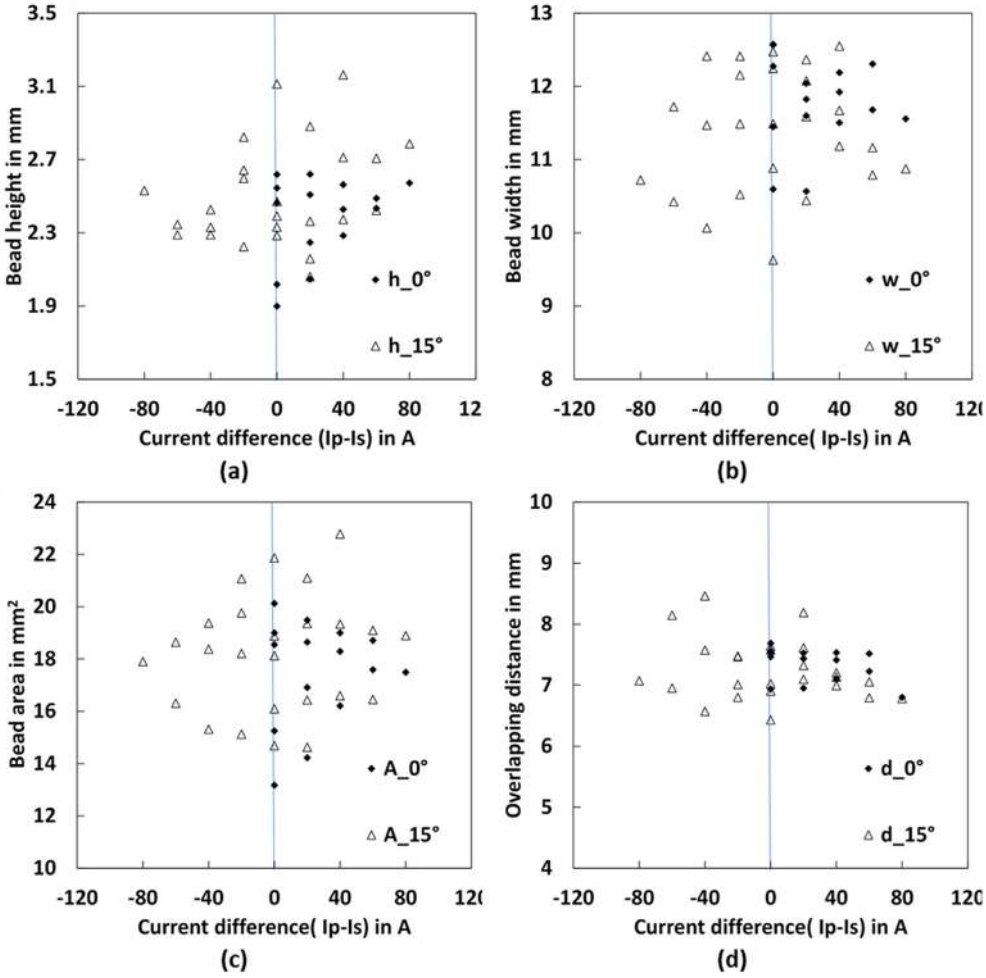

Fig. 12. Effect of welding parameters on weld bead area and critical offset.

concentration surrounding the higher current density (Sharma et al., 2008b). Also, the primary electrode that acts on the new surface stabilizes at a higher current value. The effect of the current difference can be seen in Fig. 12. The bead height (Fig. 12a) and bead area (Fig. 12c) increase with a positive current difference (*Ip > Is)*, while such dominance is not visible for the weld width (Fig. 12b) and offset (Fig. 12d). The torch inclination towards the primary side and a higher primary current complement each other. The primary electrode needs a higher current density to overcome the colder environment surrounding it. With the smaller electrode extension, the heat required for electrode melting reduces, and enough heat is available for heating the cold surrounding. From the above discussion, it is clear that the torch orientation and welding currents play a vital role in determining bead characteristics – width, height, area, and offset.

4.3. Predictive models of bead characteristic and bead offset

4.3.1. Predictive models

The bead height, offset distance, and bead area are the prerequisite weld attributes to predict the number of passes (Eq. (24)) and material wastage (Eq. (28)). The weld attributes are functions of the welding process parameter. A functional relation between the attributes and the process parameters is essential to relate the number of passes and material wastage with the welding process conditions. The relations are obtained via stepwise regression analysis and given as follows:

$$h = 0.01722I_s + 0.000018{I_p}^2 - 0.000041{I_s}^2 + 0.00007I_p{}^*\alpha \quad (29a)$$

Table 2
Model statistics.

Weld bead parameters	Standard error	R^2	R^2 (adj.)	R^2 (predictive)
Height (*h*)	0.1445	99.71%	99.66%	99.62%
Total bead area (a)	0.8530	99.80%	99.78%	99.76%
offset (*d*)	0.2684	99.88%	99.86%	99.85%

$$A = 0.05633I_p + 0.040005I_S + 0.0578\alpha \quad (30)$$

$$d = 0.06475I_p + 0.00878I_s - 0.01462\alpha - 0.000175{I_p}^2 \quad (31)$$

The models' accuracy is evident from the lower value of standard errors and the high value of the coefficient of determination (R^2), as shown in Table 2. The values of R^2, R^2 (adjusted) and R^2 (predicted) are more than 99% for all the models.

4.3.2. Model validation

The models are validated by plotting the predicted against the actual bead geometry values, as shown in Fig. 13. The models (Eqs. (29)–(31)) were developed with 80% of the available data. The rest, 20%, were used to validate the models. A comparison of actual and predicted values for the model and validation data for the three models is shown in Fig. 13. The predicted data for all the experiments are within the 10% error band. The agreement between actual and predicted data ensures the correctness of the models. Compared to the previous results of the weld bead models, the present model offers improvement in predictability. For

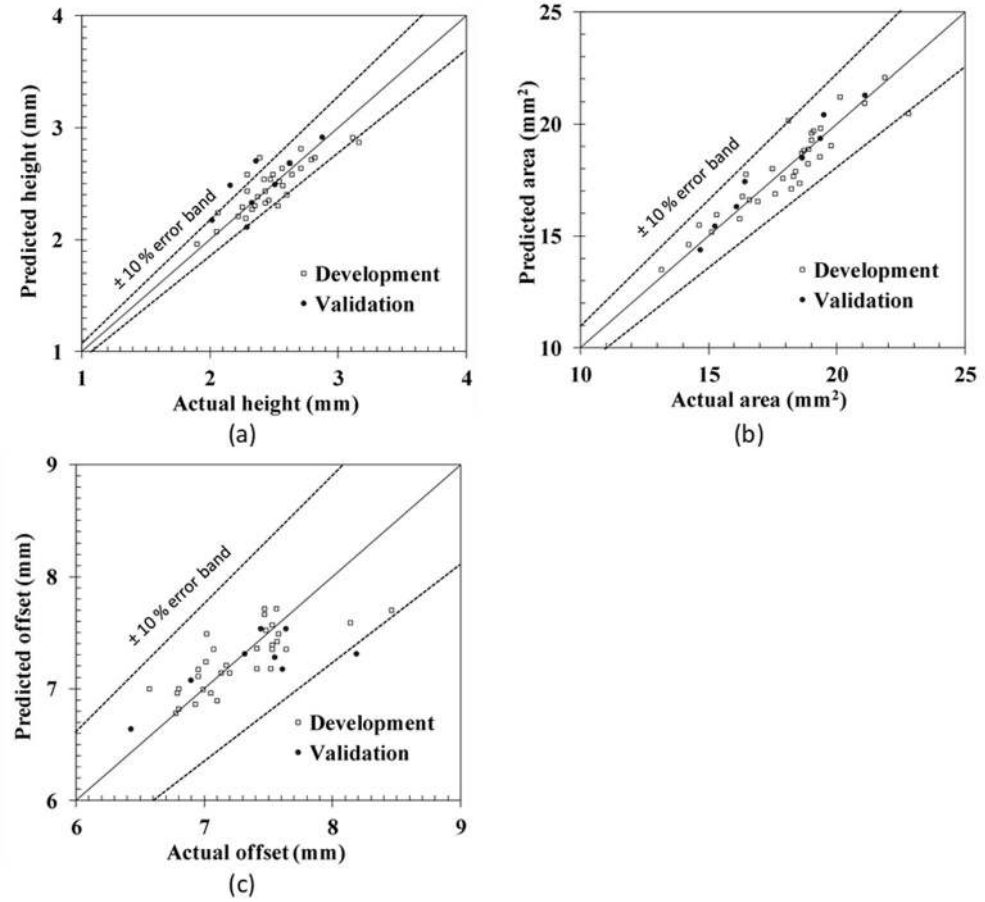

Fig. 13. Comparison of actual and predicted (a) height, (b) area, and (c) offset distance.

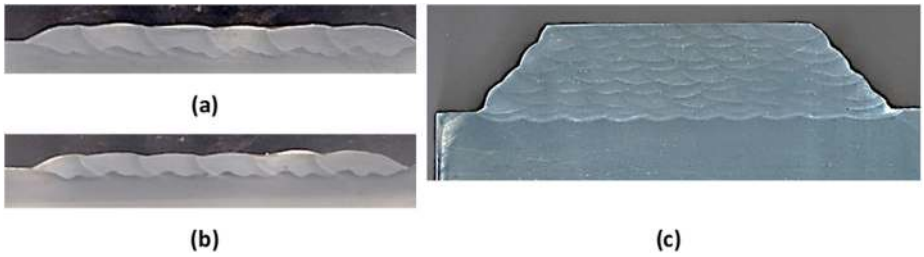

Fig. 14. Single-layer and multi-layer depositions.

example, Suryakumar et al. (2011) found that the maximum error in the first layer thickness (i.e. bead height) was 16.03%, while Sharma et al. (2015) found that the maximum error in the prediction of bead area was up to 17.47%.

4.4. Accuracy of the asymmetric weld overlap model

The developed model's efficacy is further confirmed by single-layer and multi-layer depositions, as shown in Fig. 14. The multi-layer component was produced with a 180–180 A welding current with a 15° torch inclination, a case of minimal surface waviness with a standard deviation of 0.1 mm, as shown in Table 3. The bi-polynomial weld bead profile obtained the offset. The single-layer components are reasonably flat. The multi-pass multi-layer component is without visible defects, as shown in the corresponding cross-sections in Fig. 14a and b.

Despite the bottom of the layer where the substrate melts being quite wavy (Fig. 14a and b), the welds laid at a critical offset distance fill the valley in between and create an even surface. The layers undergo partial melting and solidification when the successive layers are laid.

When compared with the previous investigations, the asymmetric weld bead model shows improvement in flatness. For example, the standard deviation of the height from 0.1 mm in the first layer increases only to 0.26 mm in the tenth layer. On the other hand, the standard deviation with a single-wire symmetric bead calculated from the surface waviness (available in Ding et al., 2015a) is 0.32 mm in the first layer increases to 0.43 mm in the fifth layer (Fig. 15). Previous investigations used the symmetric bead for different welding-based AM processes. For symmetric beads, the offset depends on the width of a single bead (Ding et al., 2015b) and can be represented in terms of the percentage of bead width (%w). Various symmetric bead profiles have different critical offsets (d), such as parabolic arc (66.7%w) (Suryakumar et al., 2011), sine function (63.66%w) (Cao et al., 2011), and circular and elliptical arc (78.57%w) (Zhang et al., 2014; Jhavar et al., 2014). However, in asymmetric beads, the value of d cannot be fixed only by the width as the weld bead shape also depends on the profile coefficients (Eq. (21)). In turn, the value of d in terms of %w ranges from 57.79% to 69.47% for

Table 3
Layer profiles at different welding conditions.

Inclination	Primary current (A)	Secondary current (A)	Layer profile	mean ± standard deviation
0°	140	140		1.96 ± 0.21
0°	180	140		2.10 ± 0.22
0°	180	180		2.18 ± 0.10
15°	140	140		2.13 ± 0.21
15°	180	140		2.20 ± 0.30
15°	180	180		2.19 ± 0.10
15°	140	180		2.29 ± 0.21
15°	180	220		2.15 ± 0.47

(all measurements in mm)

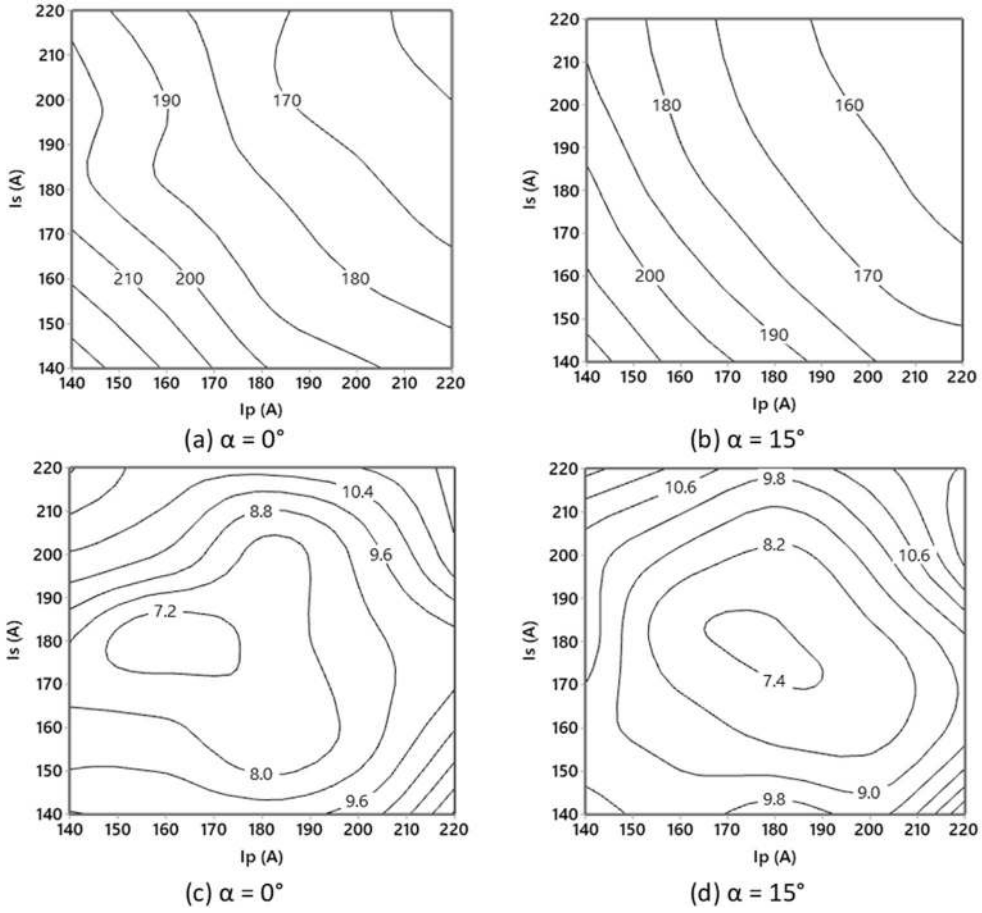

Fig. 15. Process effects on the number of passes (a and b) and material wastage (c and d).

transverse welds obtained in this investigation. For these values of *d*, the obtained surfaces are quite flat. The welding conditions have a minor impact on the surface waviness provided that the welds are offset per the *d* that is responsive to the welding conditions. The waviness increases at higher currents (180–220 A) and a higher inclination (15°). The transverse inclination of the welding torch creates a difference in CTWDs of the electrodes. A higher current in the welding wire on the inclined side generates more substantial arc pressure as low CTWDs, and high currents are both favourable to increase the arc pressure. The arc pressure forces the molten metal to blow away from the weld pool at the

preceding weld bead interface.

4.5. T^2WAAM process design

In the fabrication of components by the WAAM process, the total number of passes (N) and the percentage of material wastage ($\%M_W$) are crucial. The reduction in N brings down the fabrication time. The weld bead cross-section plays a significant role in calculating N and $\%M_W$. The welding current profoundly impacts the weld bead cross-section. An increase in the current may reduce N but, at the same time, may also affect the material loss. To apprehend the effect of the process parameters (I_p,I_s, and α), a case study is conducted on a trapezoidal block, as shown in Figs. 8 and 13, with H = 20 mm, B = 100 mm, and θ = 50°. The effects of the process conditions on the number of passes (Eq. (24)) and material waste (Eq. (28)) are shown in Fig. 15.

The increase in the current (I_p or I_s) results in a decrease in the number of passes (Fig. 15a and b), which is expected because of the increase in the deposition rate with an increase in the current. For the same reason, the torch inclination (α = 15°) brings down the material waste when compared with no torch inclination (α = 0°). The material waste is an aggregate function of A, d, and h. The change in welding currents balances out so that the extreme value of currents (too high and too low) increases the wastage, as shown in Fig. 15c and d. The material wastage minimizes at the moderate value of the primary and secondary currents. Unlike the number of passes, the torch inclination does not impact the material wastage; however, an inclined torch (α = 15°) shifts the minimum material wastage from a primary welding current of 150–180 A to 170–190 A that, in turn, helps reduce the number of passes. The interplay between process parameters and outcomes (e.g. material wastage and the number of passes in this investigation) necessitates the optimization of the process parameters. The comprehensive approach developed in this investigation can be used as a decision-making tool for WAAM process optimization. The developed approach can also be used when the large parts are additively manufactured using adaptive parameters for filling the varying cross-sections of layers of the AM process (Ding et al., 2016 a, b).

5. Conclusions

This investigation demonstrates the traverse twin-wire welding process's efficacy in obtaining high deposition rates without any significant loss in accuracy by exploiting its weld bead's asymmetric nature. This is aided by an integrated process and product design for twin-wire robotic WAAM by analyzing the weld bead profile and bead overlap. The following conclusions are derived from this study:

1. The weld bead is asymmetrical in transverse twin-wire GMAW, unlike the symmetrical profile of single-wire and tandem twin-wire welding. The bi-polynomial fourth-order curve fits well with the twin-wire welds. A weld bead overlapping model of the asymmetric weld bead is presented, making twin-wire transverse welding a potential candidate for large-scale AM. Compared to the conventional flat-top and critical valley models, which are limited to asymmetric weld bead, the current bi-polynomial fourth-order model can simulate asymmetric weld beads. As a result, the multi-pass layer's flatness significantly improves and maintained for many number of layers.
2. A flat layer can be produced by overlapping asymmetric twin-wire weld beads; however, the offset is a function of the welding parameters (welding currents and torch inclination), unlike the previous investigations that suggest an offset as a fixed proportion of the weld width. The total number of passes and material wastage in the WAAM process are not associated monotonically with the welding current. The variation trend is coupled with the shape and size of the component cross-section.
3. The process models of the weld bead shape and the offset can be integrated with the product features to assess the time for fabrication and post-machining material wastage. Such integration is apt to act as a decision-making tool for the shop-floor applications.
4. The results of this investigation are of fundamental importance. They would have a far-reaching impact on the economic consideration of the WAAM process by saving materials and time through the reduction in the total number of passes and a closer fit to the profile of the component.

Declaration of competing interest

The authors declare that they have no known competing financial interests or personal relationships that could have appeared to influence the work reported in this paper.

Acknowledgement

Acknowledgements are due to the Indian Institute of Technology Hyderabad and KU Leuven for providing support towards experimental and analytical work, respectively.

Appendix 1. Polynomial coefficients

					Primary				Secondary			
	Ip (A)	*Is* (A)	(α)	*h*	*a1*	*a1*	*a3*	*a4*	*a1*	*a1*	*a3*	*a4*
1	140	140	0	1.90	0.3056	0.2599	0.0985	0.0091	−0.1909	0.1040	−0.0584	0.0061
2	160	140	0	2.05	0.0771	−0.0284	0.0345	0.0054	−0.0992	0.1137	−0.0594	0.0055
3	160	160	0	2.02	0.1298	0.0902	0.0512	0.0050	−0.1239	0.1084	−0.0586	0.0058
4	180	140	0	2.37	−0.0840	−0.0992	0.0003	0.0006	−0.1580	−0.0391	−0.0110	0.0015
5	180	160	0	2.25	0.1291	0.1214	0.0635	0.0061	−0.1657	0.1504	−0.0903	0.0100
6	180	180	0	2.47	0.2014	0.0577	0.0405	0.0042	−0.1045	0.0384	−0.0369	0.0038
7	200	140	0	2.15	0.2036	0.1453	0.0648	0.0060	−0.2224	0.1668	−0.0752	0.0072
8	200	160	0	2.43	0.1926	0.0950	0.0512	0.0049	−0.1438	0.0273	−0.0270	0.0025
9	200	180	0	2.54	0.1136	0.0230	0.0285	0.0028	−0.2023	0.0924	−0.0530	0.0053
10	200	200	0	2.54	0.0749	−0.0544	0.0118	0.0018	−0.0821	−0.0139	−0.0195	0.0022
11	220	140	0	2.57	0.1103	−0.0266	0.0264	0.0037	−0.0407	−0.0459	−0.0280	0.0041
12	220	160	0	2.49	0.0551	−0.0309	0.0225	0.0030	−0.0404	−0.0370	−0.0163	0.0021
13	220	180	0	2.56	0.0690	−0.0169	0.0213	0.0025	−0.0938	−0.0317	−0.0199	0.0026
14	220	200	0	2.62	0.0940	−0.0608	0.0080	0.0014	−0.0449	−0.0550	−0.0068	0.0009
15	220	220	0	2.56	0.0895	−0.0064	0.0203	0.0021	−0.2068	0.0361	−0.0298	0.0030
16	140	140	15	2.29	0.2615	0.2582	0.1420	0.0164	−0.2873	0.3385	−0.1702	0.0191
17	140	160	15	2.22	0.1051	0.0862	0.0554	0.0054	−0.2619	0.1869	−0.1037	0.0118

(*continued on next column*)

(*continued*)

					Primary				Secondary			
	Ip (A)	*Is* (A)	(α)	*h*	*a1*	*a1*	*a3*	*a4*	*a1*	*a1*	*a3*	*a4*
18	140	180	15	2.33	0.0785	0.0524	0.0565	0.0062	−0.1998	0.1683	−0.1078	0.0127
19	140	200	15	2.35	0.1593	0.1018	0.0679	0.0071	−0.1674	0.1093	−0.0609	0.0059
20	140	220	15	2.53	0.1459	0.0157	0.0360	0.0037	−0.1105	0.0369	−0.0332	0.0030
21	160	140	15	2.06	0.1384	0.1145	0.0750	0.0082	−0.0794	0.0987	−0.0617	0.0062
22	160	160	15	2.33	0.0818	0.0245	0.0337	0.0033	−0.2769	0.1797	−0.0957	0.0106
23	160	180	15	2.60	0.1216	−0.0101	0.0357	0.0047	−0.0983	0.0335	−0.0434	0.0048
24	160	200	15	2.43	0.1495	0.0656	0.0432	0.0040	−0.1794	0.1066	−0.0524	0.0047
25	160	220	15	2.29	0.2284	0.2615	0.1008	0.0089	−0.0810	0.0967	−0.0608	0.0060
26	180	140	15	2.37	0.1909	0.0689	0.0549	0.0063	−0.0795	0.0162	−0.0331	0.0036
27	180	160	15	2.16	0.0843	0.0595	0.0387	0.0036	−0.1891	0.1429	−0.0752	0.0078
28	180	180	15	2.47	0.0529	−0.0292	0.0163	0.0020	−0.1205	0.0288	−0.0350	0.0037
29	180	200	15	2.64	0.0984	−0.0556	0.0096	0.0015	−0.0646	−0.0315	−0.0143	0.0017
30	180	220	15	2.29	0.2282	0.1830	0.0702	0.0060	−0.2586	0.2065	−0.0712	0.0057
31	200	140	15	2.42	0.1440	0.0492	0.0459	0.0049	−0.1977	0.1052	−0.0702	0.0078
32	200	160	15	2.58	0.0012	−0.0463	0.0176	0.0022	−0.1358	0.0184	−0.0351	0.0040
33	200	180	15	2.23	0.1844	0.1377	0.0668	0.0065	−0.1295	0.1260	−0.0600	0.0055
34	200	200	15	2.39	0.0110	−0.0407	0.0145	0.0019	−0.0440	−0.0502	−0.0147	0.0022
35	200	220	15	2.82	0.0237	−0.0937	0.0046	0.0014	−0.1416	0.0156	−0.0315	0.0034
36	220	140	15	2.79	0.2035	0.0096	0.0306	0.0031	−0.1678	0.0547	−0.0502	0.0054
37	220	160	15	2.71	0.0507	0.0044	0.0360	0.0040	−0.1775	0.0221	−0.0424	0.0050
38	220	180	15	3.16	0.0484	−0.0366	0.0224	0.0028	−0.0310	−0.1689	0.0015	0.0021
39	220	200	15	2.88	0.1640	0.0029	0.0258	0.0027	−0.0934	−0.0231	−0.0258	0.0032
40	220	220	15	3.11	0.1533	0.0427	0.0555	0.0063	0.0154	−0.1124	−0.0137	0.0030

References

Aiyiti, W., Zhao, W., Lu, B., Tang, Y., 2. Investigation of the overlapping parameters of MPAW-based rapid prototyping. Rapid Prototyp. J. 12 (3), 165–172. https://doi.org/10.1108/13552540610670744.

Cao, Y., Zhu, S., Liang, X., Wang, W., 2011. Overlapping model of beads and curve fitting of bead section for rapid manufacturing by robotic MAG welding process. Robot. Comput. Integrated Manuf. 27 (3), 641–645.

Cui, P.Z., 2007. Research on Remanufacturing Modeling and Forming Path Planning Based on the Robot. Doctoral dissertation. The Academy of Armored Forces Engineering, Beijing, China.

Datta, S., Bandyopadhyay, A., Pal, P.K., 2008. Modeling and optimization of features of bead geometry including percentage dilution in submerged arc welding using mixture of fresh flux and fused slag. Int. J. Adv. Manuf. Technol. 36 (11–12), 1080–1090.

Ding, D., Pan, Z., Cuiuri, D., Li, H., 2015a. A multi-bead overlapping model for robotic wire and arc additive manufacturing (WAAM). Robot. Comput. Integrated Manuf. 31, 101–110.

Ding, D., Pan, Z., Cuiuri, D., Li, H., 2015b. A practical path planning methodology for wire and arc additive manufacturing of thin-walled structures. Robot. Comput. Integrated Manuf. 34, 8–19.

Ding, D., Pan, Z., Cuiuri, D., Li, H., van Duin, S., Larkin, N., 2016a. Bead modelling and implementation of adaptive MAT path in wire and arc additive manufacturing. Robot. Comput. Integrated Manuf. 39, 32–42.

Ding, D., Pan, Z., Cuiuri, D., Li, H., Larkin, N., 2016b. Adaptive path planning for wire-feed additive manufacturing using medial axis transformation. J. Clean. Prod. 133, 942–952.

Feng, Y., Zhan, B., He, J., Wang, K., 2018. The double-wire feed and plasma arc additive manufacturing process for deposition in Cr-Ni stainless steel. J. Mater. Process. Technol. 259, 206–215.

Gu, J., Bai, J., Ding, J., Williams, S., Wang, L., Liu, K., 2018. Design and cracking susceptibility of additively manufactured Al-Cu-Mg alloys with tandem wires and pulsed arc. J. Mater. Process. Technol. 262, 210–220.

Hackenhaar, W., Mazzaferro, J.A., Montevecchi, F., Campatelli, G., 2020. An experimental-numerical study of active cooling in wire arc additive manufacturing. J. Manuf. Process. 52, 58–65.

Jhavar, S., Jain, N.K., Paul, C.P., 2014. Enhancement of deposition quality in micro-plasma transferred arc deposition process. Mater. Manuf. Process. 29 (8), 1017–1023.

Kumar, M., Moinuddin, S.Q., Kumar, S.S., Sharma, A., 2020. Discrete wavelet analysis of mutually interfering co-existing welding signals in twin-wire robotic welding. J. Manuf. Process. https://doi.org/10.1016/j.jmapro.2020.04.048.

Li, Y., Li, X., Zhang, G., Horváth, I., Han, Q., 2020. Interlayer closed-loop control of forming geometries for wire and arc additive manufacturing based on fuzzy-logic inference. J. Manuf. Process.

Martina, F., Ding, J., Williams, S., Caballero, A., Pardal, G., Quintino, L., 2019. Tandem metal inert gas process for high productivity wire arc additive manufacturing in stainless steel. Additive Manufacturing 25, 545–550.

Moinuddin, S.Q., Sharma, A., 2015. Arc stability and its impact on weld properties and microstructure in anti-phase synchronized synergic-pulsed twin-wire gas metal arc welding. Mater. Des. 67, 293–302.

Moinuddin, S.Q., Kapil, A., Kohama, K., Sharma, A., Ito, K., Tanaka, M., 2016. On process–structure–property interconnection in anti-phase synchronized twin-wire GMAW of low carbon steel. Sci. Technol. Weld. Join. 21 (6), 452–459.

Qi, Z., Cong, B., Qi, B., Sun, H., Zhao, G., Ding, J., 2018. Microstructure and mechanical properties of double-wire+ arc additively manufactured Al-Cu-Mg alloys. J. Mater. Process. Technol. 255, 347–353.

Qi, Z., Qi, B., Cong, B., Sun, H., Zhao, G., Ding, J., 2019. Microstructure and mechanical properties of wire+ arc additively manufactured 2024 aluminum alloy components: as-deposited and post heat-treated. J. Manuf. Process. 40, 27–36.

Queguineur, A., Marolleau, J., Lavergne, A., Rückert, G., 2020. Evaluation of tandem controlled short-circuit GMAW for improved deposition in additive manufacture of large Nickel Aluminium Bronze naval components. Welding in the World, pp. 1–7.

Reddy, S., Kumar, M., Panchagnula, J.S., Parchuri, P.K., Kumar, S.S., Ito, K., Sharma, A., 2019. A new approach for attaining uniform properties in build direction in additive manufactured components through coupled thermal-hardness model. J. Manuf. Process. 40, 46–58.

Sharma, A., Arora, N., Mishra, B.K., 2008a. A practical approach towards mathematical modeling of deposition rate during twin-wire submerged arc welding. Int. J. Adv. Manuf. Technol. 36 (5–6), 463–474.

Sharma, A., Arora, N., Mishra, B.K., 2015. Mathematical model of bead profile in high deposition welds. J. Mater. Process. Technol. 220, 65–75.

Sharma, A., Arora, N., Mishra, B.K., 2008b. Mathematical modeling of flux consumption during twin-wire welding. Int. J. Adv. Manuf. Technol. 38 (11–12), 1114–1124.

Shi, J., Li, F., Chen, S., Zhao, Y., Tian, H., 2019a. Effect of in-process active cooling on forming quality and efficiency of tandem GMAW–based additive manufacturing. Int. J. Adv. Manuf. Technol. 101 (5–8), 1349–1356.

Shi, J., Li, F., Chen, S., Zhao, Y., 2019b. T-GMAW based novel Multi-node trajectory planning for fabricating grid stiffened panels: an efficient production technology. J. Clean. Prod. 238, 117919.

Somashekara, M.A., Suryakumar, S., 2017. Studies on dissimilar twin-wire weld-deposition for additive manufacturing applications. Trans. Indian Inst. Met. 70 (8), 2123–2135.

Suryakumar, S., Karunakaran, K.P., Bernard, A., Chandrasekhar, U., Raghavender, N., Sharma, D., 2011. Weld bead modeling and process optimization in hybrid layered manufacturing. Comput. Aided Des. 43 (4), 331–344.

Wu, B., Pan, Z., Ding, D., Cuiuri, D., Li, H., Xu, J., Norrish, J., 2018. A review of the wire arc additive manufacturing of metals: properties, defects and quality improvement. J. Manuf. Process. 35, 127–139.

Xiong, J., Zhang, G., Gao, H., Wu, L., 2013. Modeling of bead section profile and overlapping beads with experimental validation for robotic GMAW-based rapid manufacturing. Robot. Comput. Integrated Manuf. 29 (2), 417–423.

Xiong, J., Zhang, G., Zhang, W., 2015. Forming appearance analysis in multi-layer single-pass GMAW-based additive manufacturing. Int. J. Adv. Manuf. Technol. 80 (9–12), 1767–1776.

Zhang, Y., Chen, Y., Li, P., Male, A.T., 2003. Weld deposition-based rapid prototyping: a preliminary study. J. Mater. Process. Technol. 135 (2–3), 347–357.

Zhang, K., Wang, S., Liu, W., Shang, X., 2014. Characterization of stainless steel parts by laser metal deposition shaping. Mater. Des. 55, 104–119.